MIT Open Access Articles

High-throughput in vivo vertebrate screening

Citation	Pardo-Martin, Carlos et al. "High-throughput in Vivo Vertebrate Screening." Nature Methods 7.8 (2010): 634–636.
As Published	http://dx.doi.org/10.1038/nmeth.1481
Publisher	Nature Publishing Group
Version	Author's final manuscript
Citable link	http://hdl.handle.net/1721.1/73602
Terms of Use	Creative Commons Attribution-Noncommercial-Share Alike 3.0
Detailed Terms	http://creativecommons.org/licenses/by-nc-sa/3.0/

High-throughput *in vivo* vertebrate screening

Carlos Pardo-Martin[1,2,3,5], **Tsung-Yao Chang**[1,5], **Bryan Kyo Koo**[1], **Cody L. Gilleland**[1], **Steven C. Wasserman**[4], and **Mehmet Fatih Yanik**[1,4,*]

[1]Department of Electrical Engineering and Computer Science, Massachusetts Institute of Technology (MIT), Cambridge, MA 02139.

[2]School of Engineering and Applied Sciences, Harvard, Cambridge, MA 02138.

[3]Division of Health Sciences and Technology, MIT, Cambridge, MA 02139.

[4]Department of Biological Engineering, MIT, Cambridge, MA 02139.

Abstract

We demonstrate a high-throughput platform for cellular-resolution *in vivo* pharmaceutical and genetic screens on zebrafish larvae. The system automatically loads animals from reservoirs or multiwell plates, and positions and orients them for high-speed confocal imaging and laser manipulation of both superficial and deep organs within 19 seconds without damage. We show small-scale test screening of retinal axon guidance mutants and neuronal regeneration assays in combination with femtosecond laser microsurgery.

Small size, optical transparency of complex organs, and ease of culture make the zebrafish (*Danio Rerio*) larva an ideal organism for large-scale *in vivo* genetic and chemical studies of many processes that cannot be replicated *in vitro*. Zebrafish models of several human diseases have been developed[1-5]. Lead compounds discovered by screening chemical compound libraries for efficacy in zebrafish disease models have been useful for pharmaceutical discovery due to the high level of conservation of drug activity between mammals and zebrafish[1-5].

Visualizing most zebrafish organs requires manipulating and properly orienting the animals. Even with confocal or two-photon microscopy, optical access is often impeded by pigmentation, by intervening organs such as eyes and heart, or by the highly autofluorescent yolk sac. Current methods to address these challenges involve treatment with the toxic chemical phenylthiourea to suppress pigmentation[6], manually transferring animals from multiwell plates or reservoirs, and manually orienting them in viscous media such as agar. These processes are too slow and unreliable for high-throughput screens To improve the throughput and complexity of zebrafish screens, we developed the vertebrate automated screening technology (VAST) that automatically manipulates and images animals on the fly, eliminating the need for any manual handling (Fig. 1 and Online Methods).

Each cycle of VAST includes the following steps: loading, detection, positioning, orienting, focusing, imaging, laser manipulation, and dispensing. Such an automated system makes both genetic and pharmaceutical whole-organism screens possible[7] (Supplementary Fig. 1). During loading, the system extracts larvae either from a multiwell plate or a reservoir. A high-speed photodetection system composed of a photodiode and two LEDs discerns the entry of larvae into the loading tube. The photodiode senses transmitted light from one LED and scattered light from the other LED. By simultaneously monitoring both the transmission and scattering signals, the system discriminates larva from air bubbles and debris with 100% reliability ($n = 1000$). After loading and photodetection, the larva moves from the larger loading tube into a capillary[8,9] positioned within the field-of-view (FOV) of an optical imaging and manipulation system. The capillary has a refractive index similar to water, allowing the use of high numerical-aperture (NA) water-immersion objectives that require short working distances. Using a fast camera and an automated image processing algorithm, the larva is coarsely positioned by the syringe pump. Next, a 3-axis stage automatically moves the capillary assembly to precisely position the larva's head at the center of the FOV. The larva is then rotationally oriented by a pair of stepper motors. Thus, larvae can be arbitrarily positioned and oriented. In addition, larvae can be automatically re-oriented, thus allowing visualization of organs from multiple angles. At the end of the cycle, animals can be dispensed back into either individual wells or larger containers by executing the loading process in reverse. See Online Methods and Supplementary Fig. 2.

Larvae are imaged through two objective lenses: an upright, high-resolution water-immersion objective and an inverted air objective. This allows both wide-field fluorescence imaging and high-resolution confocal microscopy. Imaging most phenotypes requires larvae to be oriented at specific angles. For instance, the midline crossing of the Mauthner motor neuron axons that project into spinal cord is only visible when directly observed from the hindbrain (Fig 2a, 0°). At less favorable orientations, the structure is obscured. We performed a small-scale test screen on a similar phenotype – the midline crossing of retinal axon projections to the optic tectum (Fig. 2b and Supplementary Fig. 3). Screening for retinal axon misguidance mutants had previously led to the discovery of *astray* mutation in *robo2* gene[10]. Homozygous *astray* (ast/ast) zebrafish fail to exhibit proper midline crossing, while the projections are normal in heterozygous (ast/+) zebrafish. Using our system, we were able to distinguish wild type larvae from *robo2* mutants[11] with a sensitivity of 100% and specificity of 98.8% for a 96-well plate with 83 randomly seeded mutants. The 1.20% false negative error in identification of ast/ast animals was due to the rare cases of mutants with strong phenotypic similarity to wild type. The system could thus be used for large-scale chemical screens for small molecules that rescue such misguidance.

In conjunction with sample positioning and orientation, VAST also allows *in vivo* optical manipulations such as localized activation of fluorescent reporters and ion channels, uncaging of compounds, and femtosecond laser microsurgery[12] with subcellular precision. We illustrate the use of the system to study neuronal regeneration[13] following injury by laser microsurgery[14] (Fig. 3a). The lateral-neuron axon fiber bundle projecting along the trunk of a larva is visible when the larva is laterally oriented. The bundle is axotomized by focusing near-infrared femtosecond laser pulses on it. This process is semi-automated[15]: The user selects a cell body by clicking on a graphical user interface. An algorithm measures the user-specified distance from the cell body to the point of axotomy along the axon and the position stage automatically moves the selected axonal region to the focal spot of the laser for axotomy. The regenerating axonal fibers are shown at 18 and 24 hours post-axotomy in Fig. 3a. The laser pulses are delivered with high precision (1.7 μm)[12], and the subsequent response of the tissue to the laser (i.e. immediate retraction of nerve fibers) show some variability, leading to a distribution of cut sizes (8.1 ± 5.5 μm, $n = 30$, ±s.d.) (Fig. 3b). 100% of the animals recovered

from surgery within 30 minutes with no apparent morphological abnormality, and 100% of the animals survived 24 hours post surgery ($n = 30$).

A complete cycle of loading, positioning, cellular-resolution imaging, and dispensing an animal takes less than 16 seconds (Table 1). Axotomy requires an additional 2 seconds. Screening an entire multiwell plate took 31.85 minutes with an average of 19.9 seconds per well, which includes the additional interval for retracting, moving and inserting the loading apparatus, and sealing the wells. Animals can be loaded and imaged multiple times for time-lapse assays. Performed manually, assays of similar complexity require about 10 minutes per animal, and the assays are error-prone.

Zebrafish larvae are delicate and particularly susceptible to injury by tearing at sharp edges or by deformation. The most significant potential for damaging larvae occurs as they enter the loading tube at the high aspiration rates needed to achieve the desired throughput. To lessen this risk, the flow is started at a low initial rate and increased at an acceleration of $42\ \mu l \cdot s^{-2}$ until a larva is detected by the high-speed photodetector. The maximum flow rate is limited to $330\ \mu l \cdot s^{-1}$. At this maximum rate, no injury occurs while larvae are traveling within the tubing. After a larva is detected by the photodetector, the control software decreases the aspiration rate to $83\ \mu l \cdot s^{-1}$ to allow automated recognition by the camera.

We assessed the health of 450 larvae screened at 2 dpf at three different initial aspiration rates (Fig. 4a). The assessment was based on both functional and morphological criteria. At all flow rates, heartbeat and touch response matched those of controls. Tearing of yolk was never observed ($n = 450$). At the highest initial flow rate of $330\ \mu l \cdot s^{-1}$, 2.0% of the animals exhibited morphological abnormality. With a slightly slower initial aspiration rate (increasing the screening time by approximately 1 second), all health criteria matched those of controls (Fig. 4a). Post-manipulation developmental delay was measured by monitoring the time of appearance of the swimming bladder. There was no significant difference (One way ANOVA, $P = 0.94$, 3 independent experiments with $n = 50$ for each group) between the development of larvae that were manipulated by the system and control animals, even at the highest flow rates (Fig. 4b). Among the different larval age groups tested (i.e. 2-7 dpf, $n > 100$ per age), no difference in health assessment was observed.

In summary, we demonstrate a high-throughput vertebrate screening platform with cellular-resolution imaging and manipulation capabilities that should permit large-scale *in vivo* study of complex processes such as organ development, neural degeneration and regeneration, stem cell proliferation, cardiovascular, immune, endocrine, and nervous system functions, pathogenesis, cancer, and tissue specificity and toxicity of drugs.

ONLINE METHODS

High-throughput screening platform

The system can load larvae from reservoirs or multiwell plates (Fig. 1). The multiwell plate loading stage consists of 3 linear precision motors (RCA2, Intelligent Actuators). The motors are controlled by RACON 20/30 drivers (Intelligent Actuators). The loading head consists of a larva-loading and a water-supply metal tube with inner diameters of 1.0 and 0.2 mm, respectively (New England Small Tubing Inc.) inserted into a silicone rubber block. The silicon rubber block is pressed (by the loading stage motor) against the top of the multiwell plate to seal the wells. One tube aspirates the larva from the sealed well while the other tube injects water. Two fluidic valves (075P2NC12, Bio-Chem Fluidics) are used to switch the flow between the reservoirs and multiwell plate by pinching the silicone tubing ($1/32'' \text{ ID} \times 3/32''$ OD, Bio-Chem Fluidics). Larvae are driven through the system using a syringe pump (Carvo XLP6000, Tecan Systems). The photodetection system consists of a photodiode IC (OPT301,

Texas Instruments) and two LEDs (Cree Inc) aligned in transmission and reflection configurations as shown. The photodiode IC contains an integrated amplifier. The imaging system consists of a dual (upright/inverted) microscope (Eclipse Ti, Nikon (inverted), Nikon 90i Digital Imaging Head (upright)) with two light sources (Mercury lamp, Nikon). The top port of the upright microcscope is equipped with a multi-beam laser confocal scanning head (Infinity 3, VisiTech) with a 1004×1002 pixel EMCCD camera (iXon+885, Andor Technology) for high-speed confocal imaging. For high-speed image sectioning, a piezo actuator with 400 μm travel distance (P-725 PIFOC, Physik Instrumente) holds either a 10× (NA = 0.5), 16× (NA = 0.8), or 20× (NA = 1.0) water immersion lens (Nikon). A high-speed CCD camera (GX-1050, Prosilica) is connected to the inverted microscope equipped with 10× air objective lens for larva detection, position, and rotation. Two precision stepping motors (KP35FM2-044, Japan Servo Co.) hold a capillary of diameter 800 μm along its axis of rotation. The motors are controlled by a microstepping driver (BSD-02LH, Interinar Electronics). The motor and capillary assembly is mounted on a 3-axis precision stage (MP-200, Sutter Instrument) with 0.04 μm resolution along each axis. Two NiDAQ input/output data cards (PCI-6512 and PCI-6259, National Instrument) installed in a DELL OptiPlex computer control the fluidic valves, stepping motors, and read out the voltage across the photodetector.

System automation

The detailed algorithm for operation sequence of the system is shown in the flowchart of Supplementary Figure 2. The system starts by initializing syringe pumps, cameras, lamps, shutters, position stages, and motors. The fluidic valves (Fig. 1) are switched to the source of fish i.e. either multiwell plate or fish reservoir. The larva is aspirated from the selected source at a constant rate of acceleration of 42 μl s^{-2} up to a maximum speed of 330 μl s^{-1}. The photodetector is continuously sampled at 2 kHz rate via the NiDAQ PCI-6259 card until the intensity reading crosses a pre-determined threshold (the value of threshold is calibrated in advance by trial and error). Upon detection of the larva the fluidic valve is switched to the water reservoir if the larva is being loaded from the fish reservoir. The aspiration rate is subsequently decreased to 83 μl s^{-1} to avoid damaging the larva at the entrance of the capillary. The high-speed CCD at the bottom port continuously reads at 100 frames s^{-1}. The pixel intensity is averaged over the entire field-of-view, and compared to a pre-determined threshold (value of threshold is calibrated in advance by trial and error). When average pixel intensity drops below the threshold, the aspiration is stopped. The capillary is then rotated via the motors until the larva is at the desired orientation. A large field-of-view image of the gross morphology of the larva is acquired by the CCD at the bottom port. The motorized shutter of the inverted microscope (i.e. bottom shutter) is closed while that of upright microscope (top shutter) is opened. Image acquisition is switched from the bottom CCD to either the top CCD or the high-speed scanning confocal head equipped with the EMCCD. Guided by fluorescence imaging, the region of interest is located. Either confocal stacks or wide-field fluorescence images are acquired. The top shutter is closed, and the bottom shutter opened. The image acquisition is switched to the bottom port. The system is now ready for the next cycle of operation. The control software is written in Matlab. The most recent version of the software is available upon request from the authors (MF Yanik, yanik@mit.edu).

Animals

The fluorescent retinal ganglion line (astray^{ti272z} with brn3c:gap43-gfp), the fluorescent lateral neuron line, and the fluorescent mauthner line (ETj1282b:GFP) were maintained and crossed using standard techniques. All animal experiments were approved by MIT's Committee on Animal Care under protocol numbered 0309-025-12.

Axon guidance screen

Genotypically homozygous +/+ and ast/ast fish were crossed to generate ast/+ larvae. A 96-well plate was randomly and partially populated with the heterozygous ast/+ progeny. The rest of the wells were populated with the homozygous progeny of ast/ast fish. A blind screen was performed by loading the animals from multi-well plates and orienting them to visualize midline crossing as in part (a) by a $10\times$ (NA = 0.5) objective lens with long depth-of-focus in wide-field fluorescence imaging mode. Animals were blindly classified according to the observed phenotype.

Laser axotomy

A tunable femto-second laser (Mai Tai, Spectra-Physics Lasers) is guided to the upright microscope for laser axotomy as we previously described[20]. The axon fiber of GFP-expressing lateral neuron is cut 850 μm distance from the soma using ultrashort laser pulses with 780 nm wavelength, 100 fs duration, 12.7 nJ pulse energy, 80 MHz repetition rate, and 10 ms long pulse train focused by a $20\times$ (NA = 1.0) objective lens. Statistics of laser cut sizes were quantified with $40\times$ (NA = 0.8) objective lens. Surgeries were repeated on $n = 30$ animals with 100% success rate.

Assessment of animal health

The syringe was operated at three different initial aspiration rates of 165, 250, and 330 μl·s^{-1} for loading 2 dpf larvae from multiwells. $n = 450$ larvae in total were anesthetized with 0.20 mg·ml^{-1} Tricaine, loaded, and dispensed from the platform. A control group of $n = 150$ larvae from the same breed were similarly anesthetized. Health assessment was based on both functional and morphological criteria measured at t = 0, 12, 16, 20, 24, 28, 32 and 36 hours post screening. Functional criteria included visual confirmation of normal heartbeat, and reflex response to touch stimuli. Morphology criteria included bending (i.e. lordosis, kyphosis, and scoliosis) and craniofacial abnormalities. The criteria included those injuries even if the animals regenerated later.

Supplementary Material

Refer to Web version on PubMed Central for supplementary material.

Acknowledgments

REFERENCES

1. Lieschke GJ, Currie PD. Animal models of human disease: zebrafish swim into view. Nat Rev Genet 2007;8(5):353–67. [PubMed: 17440532]

2. Zon LI, Peterson RT. In vivo drug discovery in the zebrafish. Nat Rev Drug Discovery 2005;4(1):35–44.

3. Rubinstein AL. Zebrafish: from disease modeling to drug discovery. Curr Opin Drug Discov Devel 2003;6(2):218–23.

4. McGrath P, Li C. Zebrafish: a predictive model for assessing drug-induced toxicity. Drug Discovery Today 2008;13(9-10):394–401. [PubMed: 18468556]

5. Shin JT, Fishman MC. From Zebrafish to human: modular medical models. Annu. Rev. Genomics. Hum. Genet 2002;3:311–40. [PubMed: 12142362]

6. Karlsson J, Hofsten JV, Olsson PE. Generating Transparent Zebrafish: A Refined Method to Improve Detection of Gene Expression During Embryonic Development. Marine Biotech 2001;3:522–7.

7. Rohde CB, et al. Microfluidic system for on-chip high-throughput whole-animal sorting and screening at subcellular resolution. PNAS 2007;104(35):13891–5. [PubMed: 17715055]

8. Funfak A, Brosing A, Brand M, Kohler JM. Micro fluid segment technique for screening and development studies on Danio rerio embryos. Lab Chip 2007;7:1132–8. [PubMed: 17713611]

9. Buckley, et al. Zebrafish myelination: a transparent model for remyelination? Disease Models & Mechanisms 2008;1:221–8. [PubMed: 19093028]

10. Fricke C, et al. astray, a Zebrafish Homolog Required for Retinal Axon Guidance. Science 2001;292:507–10. [PubMed: 11313496]

11. Xiao T, Roeser T, Staub W, Baier H. A GFP-based genetic screen reveals mutations that disrupt the architecture of the zebrafish retinotectal projection. Development 2005;132:2955–67. [PubMed: 15930106]

12. Steinmeyer JD, Gilleland CL, Pardo-Martin C, Angel M, Rohde CB, Scott MA, Yanik MF. Construction of a femtosecond laser microsurgery system. Nature Protocol 2010;5(3):395–407.

13. Bhatt DH, Otto SJ, Depoister B, Fetcho JR. Cyclic AMP-Induced Repair of Zebrafish Spinal Circuits. Nature 2004;305:254–8.

14. Yanik MF, Cinar H, Cinar N, Chisholm A, Jin Y, Yakar AB. Neurosurgery: Functional regeneration after laser axotomy. Nature 2004;432:822. [PubMed: 15602545]

15. Zeng F, Rohde CB, Yanik MF. Subcellular precision on-chip small-animal immobilization, multi-photon imaging and femtosecond-laser manipulation. Lab Chip 2008;8:653–6. [PubMed: 18432331]
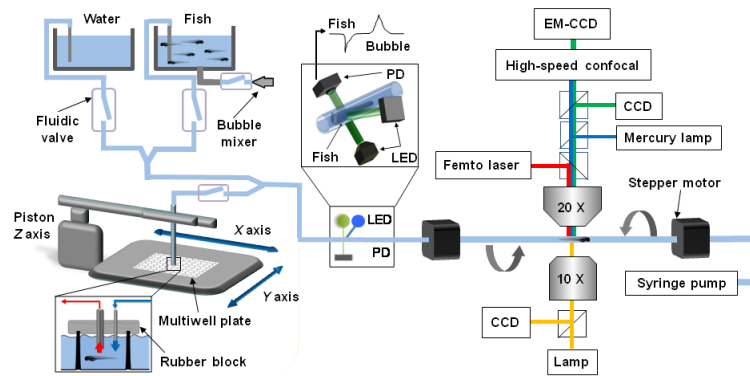
Figure 1.
Schematic of zebrafish manipulation and imaging platform. Larvae are automatically loaded to the system from either reservoirs or multi-well plates. Reservoirs are connected to the system via fluidic valves and a bubble mixer prevents the larvae from settling. The multiwell plate sits on a motorized *x-y* stage, which positions individual wells below a larva-loading (red arrow) and a water-supply (blue arrow) tube, both held by a silicone rubber block. The block seals the well surfaces as a piston moves the tubes into the wells. A photodetection system including two LEDs and one high-speed photodiode (PD) discriminates the passage of a larva from air bubbles and debris. Two stepping motors hold a capillary along its axis of rotation; this assembly is mounted on a 3-axis position stage (not shown) and held between an upright microscope for confocal imaging and an inverted microscope for bright-field imaging. A multifocal confocal head with a cooled electron-multiplying (EM) CCD camera and a second large-area CCD connected to the upright port are used for for high-speed confocal and wide-field fluorescence imaging. A high-speed CCD camera connected to the inverted port allows rapid bright-field detection and positioning of larvae. A femtosecond laser beam used for microsurgery is directed to the upper beam path by a dichroic filter and focused on the sample through the objective.
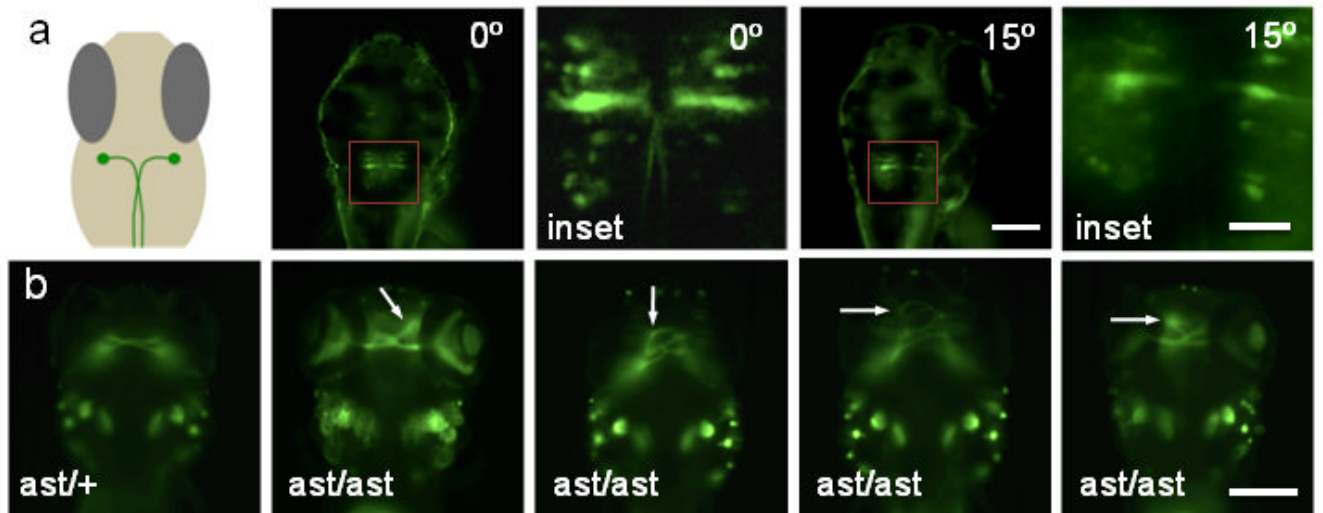
Figure 2.
Orientation, imaging, and screening of zebrafish larvae. (**a**) Schematic (left) showing the midline crossing of Mauthner axons. Right panels show confocal images of EGFP-expressing Mauthner cells at 0° and 15°. Magnified versions of marked insets are shown in each case. Scale bar, 150 μm (50 μm for insets). (**b**) Widefield fluorescence images illustrating the phenotypes distinguished in a small-scale test screen. Images show GFP-labeled axons of retinal ganglion neurons projecting to the optic tectum in larvae of the indicated genotypes. Images are representative of the phenotypes seen in mutant fish (see Supplementary Figure 3 for more examples). White arrows point to the misguided projections. Scale bar, 150 μm.
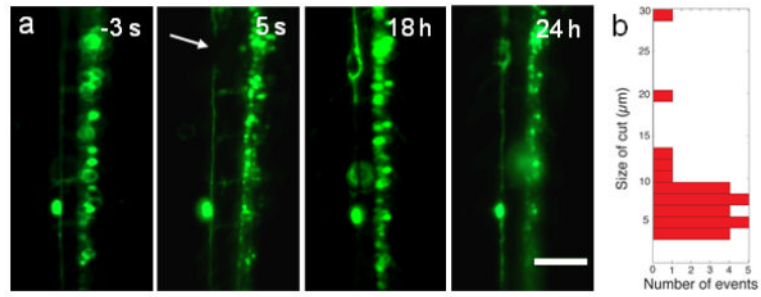
Figure 3.
Laser microsurgery and neuronal regeneration. (**a**) Wide-field fluorescence images of GFP-expressing lateral-neuron axon fibres in a 3dpf larva are shown at the indicated times pre- and post- axotomy. (**b**) The distribution of laser cut sizes is shown (*n* = 30). Scale bar, 75 μm.
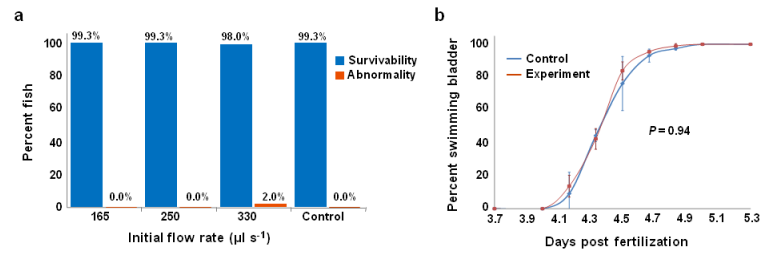
Figure 4.
Quantitative assessment of animal health. (**a**) Survival and abnormality of larvae as a function of initial flow rate ($n = 150$ for each rate). (**b**) Appearance time of swimming bladder in screened and control fish ($n = 50$).

Table 1

Average duration of screening steps

Step	Time (sec)
Loading	
from multiwell plate	2.1 ± 0.4
from reservoir	2.2 ± 0.3
From photodetector to field-of-view	2.7 ± 0.3
Positioning	2.9 ± 0.6
Orienting & focusing	5.6 ± 1.7
Microsurgery	2.1 ± 0.5
Unloading	2.5 ± 0.1

n = 150 in total, ± s.d.